

Intrinsically stretchable neuromorphic devices for on-body processing of health data with artificial intelligence

Shilei Dai^{1,2,8}, Yahao Dai^{1,8}, Zixuan Zhao^{3,4,8}, Fangfang Xia^{3,4*}, Yang Li¹, Youdi Liu¹, Ping Cheng¹, Joseph Strzalka⁵, Songsong Li¹, Nan Li¹, Qi Su¹, Shinya Wai¹, Wei Liu¹, Cheng Zhang¹, Ruoyu Zhao⁶, J. Joshua Yang⁶, Rick Stevens^{3,4}, Jie Xu⁷, Jia Huang², Sihong Wang^{1,7,9*}

¹Pritzker School of Molecular Engineering, The University of Chicago, Chicago, IL, USA;

²School of Materials Science and Engineering, Tongji University, Shanghai, China;

³Department of Computer Science, The University of Chicago, Chicago, IL, USA;

⁴Computing, Environment and Life Sciences, Argonne National Laboratory, Lemont, IL, USA;

⁵X-Ray Science Division, Argonne National Laboratory, Argonne National Laboratory, Lemont, IL, USA;

⁶Department of Electrical and Computer Engineering, University of Southern California, Los Angeles, CA, USA;

⁷Nanoscience and Technology Division, Argonne National Laboratory, Lemont, IL, USA;

⁸These authors contributed equally: Shilei Dai, Yahao Dai, Zixuan Zhao

⁹Lead contact

* Email: sihongwang@uchicago.edu, fangfang@anl.gov

Summary

For leveraging wearable technologies to advance precision medicine, personalized and learning-based analysis of continuously acquired health data is indispensable, for which neuromorphic computing could provide the most efficient implementation of artificial intelligence (AI) data processing. For realizing on-body neuromorphic computing, skin-like

stretchability is required, but yet to be combined with the suite of desired neuromorphic metrics, including linear, symmetric weight update, and sufficient state retention, for achieving high computing efficiency. Here, we report an intrinsically stretchable neuromorphic device based on an electrochemical transistor, which provides a large number (>800) of states, linear/symmetric weight update, excellent switching endurance (>100 million), good state retention (>10⁴ s), together with high stretchability of 100% strain. Further integration into a prototype array successfully realized the implementation of vector-matrix multiplication even at 100% strain. Finally, we demonstrate the feasibility of implementing AI-based classification of health signals (as exemplified by electrocardiograms) with a high accuracy that is minimally influenced by the stretched state of the neuromorphic hardware. This work breaks the ground for combining AI data analysis into skin-like wearable electronics for achieving human-integrated/mimetic intelligent systems.

Introduction

Precision medicine, the future landscape of healthcare, can provide personalized diagnosis and treatments to each individual by taking into account the underlying differences in people's genes, ages, health histories, and living environments¹. On the technological level, this futuristic vision for healthcare requires the development of two major capabilities: (1) the effective and continuous acquisition of multi-modal health data during long-term daily activities outside of clinics, for which wearable electronics emerge as the ideal solution²; and (2) the high-throughput and intelligent analysis of such complicated and large-quantity dataset for extracting the underlying personalized health patterns, which is becoming one of the main application directions of artificial intelligence (AI)³. For wearable electronics, the past decade has witnessed the rapid development of a rich collection of skin-like, stretchable designs of functional materials^{4,5}, sensors⁶, actuators⁷,

transistors⁸, and circuits⁹ that can adhere seamlessly to the human skin to provide on-body and high-fidelity measurement of various types of health data. However, for further incorporating AI data analysis, a major gap still exists on the hardware level. The efficient and secure processing of such continuously generated health data demands AI computation (Figure 1A) to happen physically next to the data-acquisition sites (i.e., sensors), to minimize the need for wireless, long-distance data transfer that typically comes with the problems of latency, insecurity, and extra power consumption^{10,11}. For such close-proximity integrations with on-skin sensors, the computing units for implementing AI data processing also need to have soft and stretchable properties, without incorporating rigid circuits, so as to achieve good wearing comfort and avoid unreliable but potentially numerous interconnections between soft and rigid parts. In particular, intrinsically stretchable designs are the most ideal choice for achieving the highest possible skin conformability and high device integration density^{8,9,12}.

Recently, a new computing paradigm—neuromorphic computing—that mimics the brain operation has been created and developed as a more suitable platform for AI, offering much lower system complexity, lower energy consumption, and faster speed. Remarkable progress has been made in neuromorphic computing based on a variety of device types, such as phase-change memory^{13,14}, atom switch devices¹⁵, memristors^{16,17}, and electrolyte-gated transistors^{18,19}. However, there hasn't been any report of intrinsically stretchable neuromorphic devices that possess the set of neuromorphic performance metrics needed for the on-body processing of health data²⁰⁻²³, which include: (1) a wide range of linear and symmetric weight updates, (2) sufficient state-retention time (>1000 s) for learning and inference, (3) excellent write endurance, (4) low variation in weight update, and (5) over 100 separable memory states. For providing all these performance characteristics, organic electrochemical transistors (OECTs) have been recently

demonstrated as the most promising device platform²⁴⁻²⁶. Towards the incorporation of stretchability onto OECTs, despite some demonstrations based on strain-engineering (i.e., rigid-island or buckling) designs^{27,28}, intrinsic stretchability has been rarely achieved^{29,30}. The very few reports up to date share two major limitations (Table S1): incomplete OECT device structures (i.e., without incorporating stretchable solid/gel-state electrolyte and stretchable gate electrode) which is not compatible for circuit-level integration; and inferior stretchable OECT performance from the use of engineered poly(3,4-ethylenedioxythiophene):polystyrene sulfonate (PEDOT: PSS). The combination of full-device stretchability and desirable neuromorphic performance for on-body AI computation has been hindered by the lack of stretchable materials across the board (including semiconductors, conductors, and dielectrics) with suitable properties for high-performance OECTs. Moreover, towards coupling mechanical stretching onto this new paradigm of analog computing and on-body AI analysis, a major challenge also lies in the lack of knowledge on the mechanical strain's influence on the implementation of artificial neural network (ANN) algorithms, which is pivotal for the further co-design of suitable AI algorithms for stretchable neuromorphic chips.

Here, through a holistic innovation in material and device designs, we report the first intrinsically stretchable neuromorphic device (Figures 1B-F) that provides all the desired computational and mechanical characteristics, including a large number (>800) of memory states, quasi-linear/symmetric weight update, excellent switching endurance (>10⁸), low variation in weight update, good state retention (>10⁴ s), and high stretchability (100% strain). These computational properties are either comparable to or even better than those of the state-of-the-art non-stretchable neuromorphic transistors (Table S2). The further integration of this device into a neuromorphic array has demonstrated the ideal implementation of the basic computation in ANN

algorithms—vector-matrix multiplication (VMM)—under the stretching to 100% strain. We also implemented different types of neural-network simulations on a large-scale array built from our stretchable neuromorphic devices, from which the training-based classifications of a representative type of health data—electrocardiogram (ECG)—were realized. With the training and inference processes carried out on the neuromorphic device operating under different strain levels from 0 to 100%, we show that the computation outcome based on Convolutional Neural Network (CNN) is not influenced by stretching. As a whole, these results from the signal-device level to the algorithm-implementation level demonstrate the promise and the possible pathway for realizing skin-like, on-body AI computation.

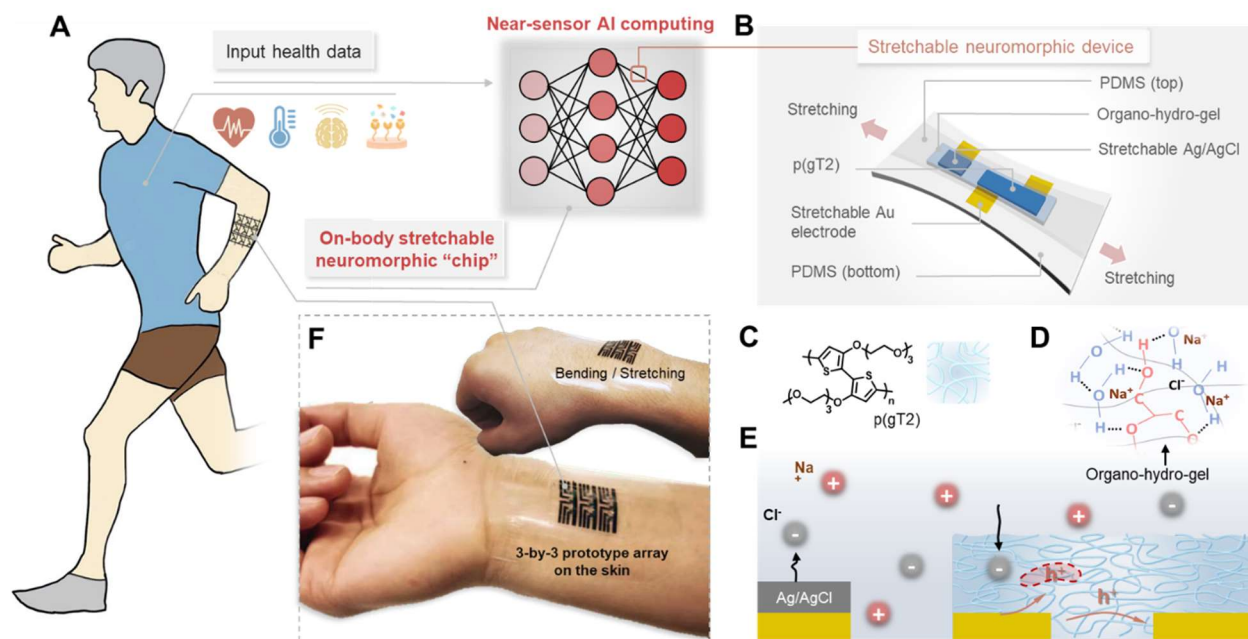


Figure 1. Stretchable neuromorphic devices for on-body processing of health data. (A) Overall role of on-body AI analysis for real-time health data processing. (B) Design of the stretchable neuromorphic device. (C) Chemical structure of the stretchable redox-active semiconducting polymer, p(gT2). (D) Organo-hydro-gel with solvated NaCl salt as the stretchable electrolyte dielectric layer. (E) Device working principle. (F) Photos of a prototype stretchable

neuromorphic “chip” attached to the human body with skin-like conformability.

Results and discussion

Material and device designs of the stretchable neuromorphic device.

Our stretchable neuromorphic device is designed with an extended-gate structure (Figure 1B) that consists of four components: a redox-active semiconducting layer, an electrolyte-type dielectric, source/drain (S/D) electrodes, and a redox-active gate electrode. We successfully incorporated the stretchability of 100% strain to each of the component materials that provide desired properties for OECT operations. For the semiconductor layer, stretchability is achieved on redox-active semiconducting polymers based on the polythiophene backbone and tri-ethylene-glycol (TEG) side chain, namely poly-[3,3'-bis(2-(2-(2-methoxyethoxy)ethoxy)ethoxy)-2,2'-bithiophene] (p(gT2)) (Figure 1C and Figures S1-2). It provides an OECT performance close to the state of the art³¹⁻³³. For the electrolyte-type dielectric layer that can form a continuous ion-transport pathway between the semiconductor layer and gate electrode, we realized the stretchability by creating a hybrid organo-hydro-gel, based on a polyacrylamide (PAAm) network swelled by a water-glycerol binary solvent (Figure 1D and Figure S3). The added NaCl inside the gel can be solvated by water and penetrate the semiconductor layer to dope the polymer semiconductor. Glycerol, which can form strong hydrogen bonding with water, is added to achieve the long-term stability of the gel dielectric by preventing dehydration and lowering the freezing point^{34, 35}. The stretchable S/D electrodes in such OECT devices need to have electrochemical stability under the doping condition of p(gT2) and high conductivity, which precludes the commonly used options of stretchable conductors made from carbon-nanotube assemblies, Ag nanowire assemblies, liquid metal, and stretchable PEDOT: PSS. We fulfilled such stability and conductivity requirements through a unique stretchable design for Au, which is vertically-grown-

nanowire-array³⁶ embedded in a PDMS substrate (Figures S4-9), which can be stretched to 100% strain while maintaining a low sheet resistance of $\sim 30 \Omega/\square$ (Figure S9). A commercially available Ag/AgCl paste was used as the stretchable redox-active gate electrode (Figure S10), which functions as a reference electrode for providing a stable electrode potential. This paste is formulated to be screen printed but can also be syringe dispensed, dipped, and sprayed. Also, this paste is very resistant to flexing, creasing, and stretching. The device built by the above set of materials enables voltage-driving redox reactions between the p(gT2) layer and the Ag/AgCl gate ($\text{AgCl} + [\text{p}(\text{gT2})] \rightleftharpoons \text{Ag} + [\text{p}(\text{gT2})]^+\text{Cl}^-$), which provides analog and non-volatile modulation of the channel's conductivity (Figure 1E). This stretchable device enabled the first realization of a skin-like neuromorphic “chip” with multiple devices (Figure 1F) that can function on the body with deformable and conformable properties.

Among all the materials, p(gT2) is the key enabler for both the high stretchability and high computing performance of the neuromorphic device. As shown in Figure 2A and Figures S11-12, a p(gT2) film can be stretched to 100% strain without any cracks, which should be mainly rendered by the relatively flexible polythiophene backbone. We used the transfer-lamination method to measure the OECT performance of p(gT2) under different strains (Figure S13). Starting from an ideal OECT performance (Figure 2B) with an on/off ratio over 10^3 and a normalized transconductance (G_m) of $(81 \pm 14) \text{ S/cm}$, the stretching processes in parallel, and perpendicular, to the channel-length direction, respectively lead to a slight increase, and a slight decrease, in G_m (Figure 2C). Upon releasing to 0% strain, G_m mostly reverts to the original value. These trends agree very well with the changes of the mobility under these stretching processes (Figure 2C and Figure S14-15), with the onset voltage of oxidation ($V_{\text{ox, onset}}$), volumetric capacitance (C^*), and the threshold voltage (V_{Th}) remaining stable (Figure S16-17). Such anisotropic response to

stretching mainly comes from the strain-induced chain alignment on this highly stretchable polymer, as confirmed by the cross-polarized optical microscopy images (Figure S18), the increase of the dichroic ratio from the polarized UV-vis spectroscopy (Figure S19), and the change in the grazing-incidence X-ray diffraction (GIXD) with incident beams in parallel and perpendicular to the strain (Figure 2D and Figure S20). The GIXD results also show moderate crystallinity of the p(gT2) polymer, which should serve as a morphological basis for the high stretchability. We can also observe the strain-induced change of mixed face-on and edge-on packing to edge-on-dominated packing.

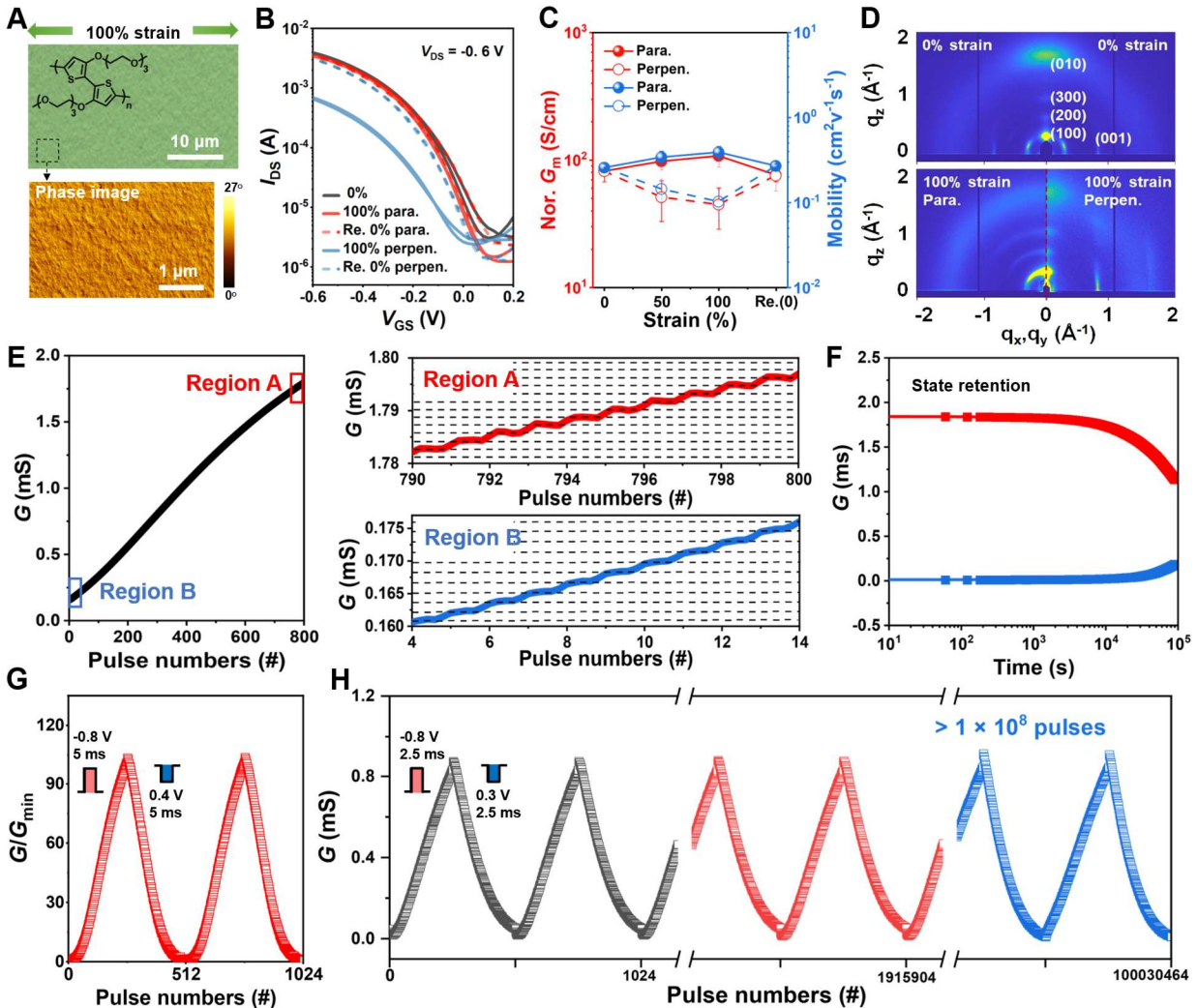


Figure 2. Core material characterization and neuromorphic functions of the stretchable neuromorphic device. (A) Optical microscopy and atom force microscopy (AFM) phase images of p(gT2) film under 100% strain. (B) Transfer curves obtained from p(gT2) film in its original and stretched state. (C) Normalized transconductance (G_m) and mobility of p(gT2) film as a function of strain. (D) GIXD 2D patterns of p(gT2) film under 0 and 100% strains. (E) Analog weight update process with 800 discrete conductance states. (F) Retention of the highest and lowest conductance states (i.e., fully potentiated and fully depressed states, respectively), with the gate disconnected from the source electrode. (G) LTP-LTD cycle under the optimized pulsing condition, giving the dynamic range over 100. (H) Endurance with more than 10^8 writes/erase pulses.

Neuromorphic computing performance at the strain-free state

With an ideal transistor-type transfer behavior (Figure S21) obtained from the fabricated fully stretchable neuromorphic device, we tested its neuromorphic-computing performance, through the two core neuromorphic properties—analogue weight update and state retention. Under an optimized pulsing condition, as many as 800 distinct conductance states can be obtained (Figure 2E), which is the highest number of states reported so far for neuromorphic devices (Table S2). This is enabled by the high volumetric capacitance of the p(gT2) semiconductor ($227 \pm 26 \text{ F/cm}^3$). Following the weight update (i.e., the “writing” process), the retention for both the fully potentiated and fully depressed states in the “reading” condition (i.e., with disconnected source and gate electrodes) can last for over 10,000 s (Figure 2F), which is sufficient for on-device training applications²⁰. When the “reading” period is further increased to 10^5 s, the accumulated decay of the states should just come from the unavoidable self-discharging behaviors of any electrochemical cells. In long-term potentiation-depression (LTP-LTD) cycles, a dynamic range ($G_{\text{max}}/G_{\text{min}}$) value greater than 100 was achieved under the optimized pulse conditions (i.e., V_{LTP} and V_{LTD}) (Figure 2G and Figure

S22). Very high linearity and symmetricity are also obtained at the same time, which, for accurate and efficient online training of ANN algorithms, could be even more important performance characteristics than the dynamic range. To examine the switching endurance of our device, we applied more than 10^8 pulses during repeated LTP—LTD cycles, and no significant degradation of the device performance can be observed (Figure 2H). We also investigate the switching speed of our device, a decent response under the pulse with a width of 500 μ s was observed (Figure S23). The switching speed can be future improved by optimizing device geometry, reducing the ionic resistance of the electrolyte, etc.²⁵ Moreover, with PDMS packaging, the on-shelf stability of our device is demonstrated for more than 4 months (Figure S24).

Neuromorphic computing performance under stretching

We then proceeded to characterize the stretchability of the device, by measuring the LTP-LTD cycles when the device is stretched stepwise from 0 to 100% strain and then released, in both parallel and perpendicular directions to the channels. As shown in Figures. 3A-B, and Figure S25, the most obvious influence of the strain is the moderate decreases of the conductance level of each updated weight, which should come from the combined effects of the device's geometry change and the strain-induced chain alignment in the semiconducting layer as described above. Upon releasing to 0% strain, these changes are mostly reversible. The further 100 cycles of stretching to 100% strain caused negligible changes to the LTP-LTD performance. On the other hand, the high degrees of linearity and symmetricity are well maintained during these stretching processes. This is quantitatively analyzed using two extracted parameters: the non-linearity index (β) and symmetricity index (Figures S26-27). As shown in Figures 3C-D and Figure S28, the stretching leads to minimal changes to the initial β around 0.2 and 1.2 (indicating high linearity) for LTP and LTD, and to the initial symmetricity index around 70 (indicating high symmetricity). In addition,

the state retention of the device at 100% strain is largely unaltered (Figure S29). These behaviors indicate the device's well-maintained capability for implementing ANN computation under large strains.

We further analyze the linearity in detail from 50 repeated LTP-LTD cycles (Figures 3E-F) under both 0 and 100% strain. At each conductance state (G) during repeated LTP-LTD cycles (Figure S30), the weight updates (ΔG) from a single "write" pulse are extracted and analyzed using the cumulative distribution function (CDF), as:

$$CDF_G(\Delta G_x) = \int_{-1}^{\Delta G_x} p_G(\Delta G) d\Delta G_x$$

in which $p_G(\Delta G)$ is the probability distribution for ΔG under a certain conductance state G . As shown by the heat plots of CDF for the ΔG distribution (Figures 3G-J), our device maintains high linearity and repeatability (i.e., low weight update distribution) under both pristine and stretched conditions.

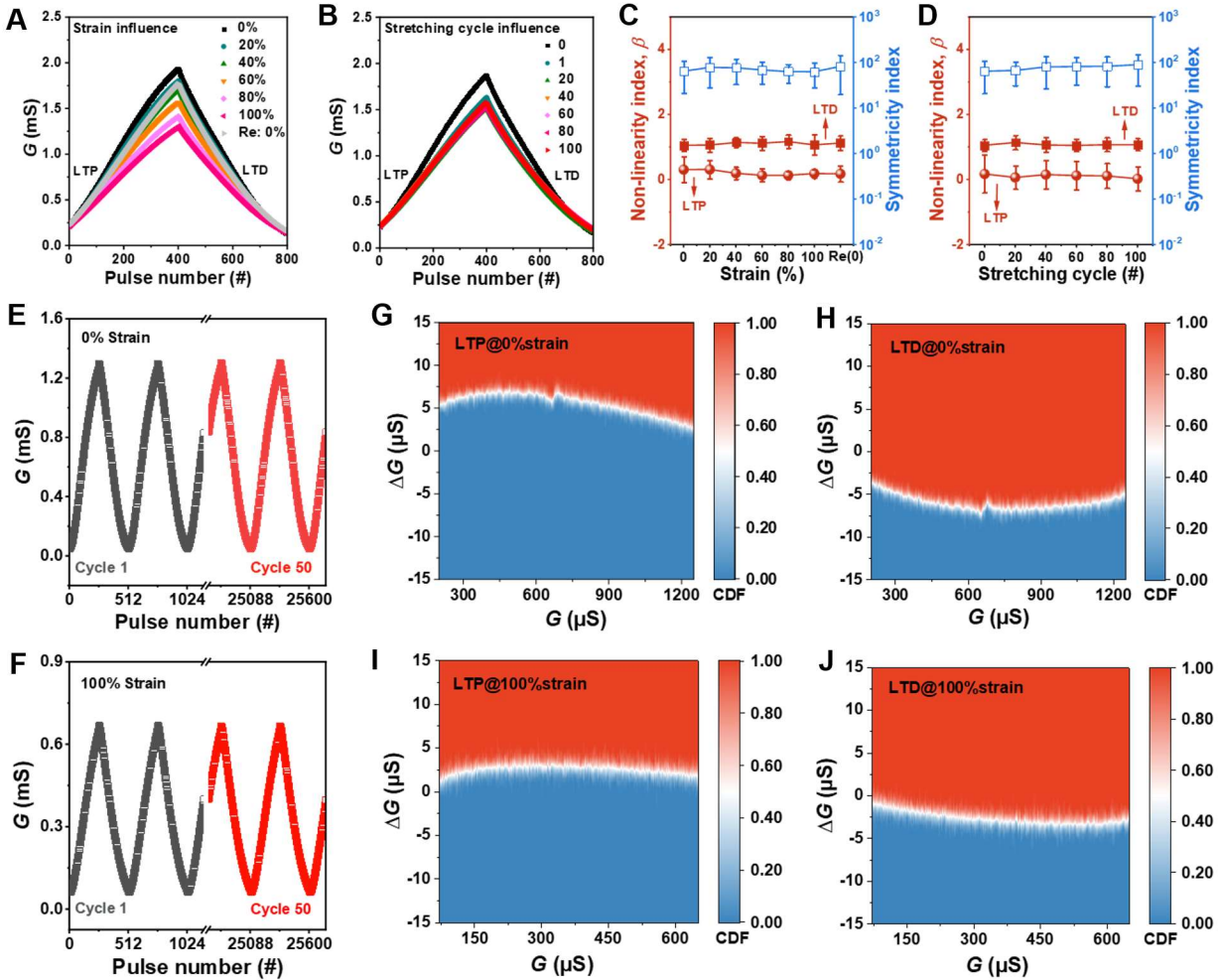


Figure 3. Neuromorphic performance under stretching. (A-B) LTP-LTD curves of the device under stretching in parallel to the charge transport direction from 0 to 100% strain and subsequently releasing (A), and 100 continuous repeating cycles (B). (C-D) Non-linearity index, and symmetry index under different (C) strains and (D) stretching cycles in the direction parallel to the charge transport direction. (E-F) Reproducibility of conductance change (ΔG) over 50 LTP-LTD cycles under (E) 0% and (F) 100% strain. (G-J) The cumulative distribution function (CDF) heat map shows the extract ΔG distribution from (E) and (F) at each conductance state G .

Array integration and the implementation of vector-matrix multiplication (VMM)

Next, towards using our stretchable neuromorphic device to achieve integrated neuromorphic

chips capable of implementing ANN algorithms, an important step is to integrate the single device into an array (Figure 4A) that can carry out the vector-matrix multiplication (VMM) operation (Figure 4B), which is the basic computational step in most ANN algorithms. To demonstrate this capability of our device, we fabricated a 3-by-3 prototype array (Figure 4C & Figure 1F) by patterning all the components: the p(gT2) semiconductor, the organo-hydro-gel, the stretchable Au nanowire electrodes, and the stretchable Ag/AgCl reference gate (see Experimental Procedures and Figure S31). In our design, the source electrodes from the three neuromorphic devices in each row are connected as three output lines. The measured LTP -LTD cycles from each of the 9 devices in the array all show similar performances (Figure S32) to the single device reported above. To demonstrate VMM operations, we first mapped a random set of conductance states $\{G_{ij}\}$ (Figure 4D, and Figure S33) into the 9 devices in the array. Then, different sets of input voltage signals ($V_{In,1}$, $V_{In,2}$, $V_{In,3}$) were applied to the three input lines of the array (Figure 4A). According to Kirchhoff's law, the three output currents should be the inner product between the input voltage vector and the conductance matrix, as

$$I_j = \sum_{i=1}^3 V_i \cdot G_{ij}$$

As shown in Figures 4E-F and Table S3, the measured output currents for each set of input voltage signals agree highly well with the calculated values from the above multiplication equation, under both 0 and 100% strain on the array. This confidently demonstrates that our stretchable neuromorphic array has an ideal capability in implementing VMM-based ANN algorithms, without being influenced by stretching. We expect that the device number and density for implementing the full-scale ANN algorithms can be further improved by using more sophisticated additive printing and photolithography methods for patterning each component in the array¹².

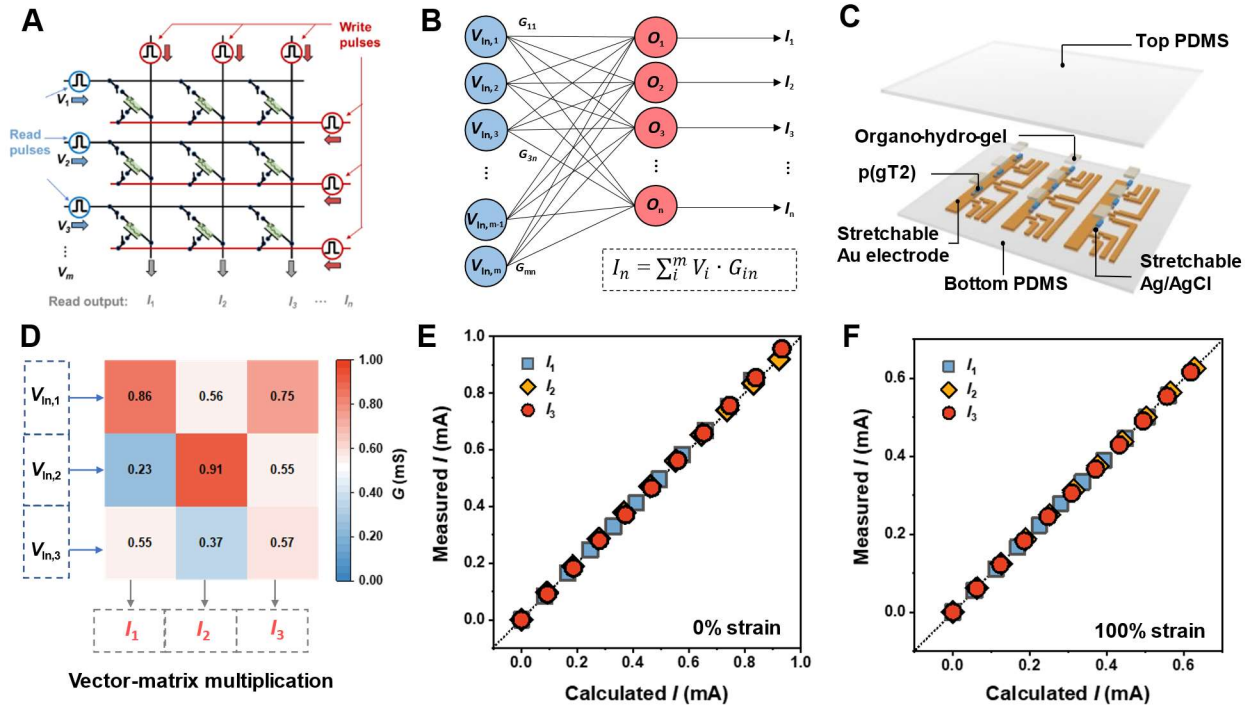


Figure 4. Stretchable neuromorphic array and its implementation of vector-matrix multiplication (VMM). (A-B) Circuit architecture (A) for the function of the neuromorphic device array in implementing VMM (B) in ANN algorithms. (C) Expanded schematic of a 3-by-3 prototype stretchable neuromorphic array. (D) In the array with the mapped conductance states. $V_{in,i}$ is the reading voltage applied to the i^{th} row of the crossbar, and I_j is the read-out current at the j^{th} column. (E-F) Corresponding relationship between measured and calculated current values from the read output column, with the array at 0% strain (E) and 100% strain (F), respectively.

Classification for ECG patterns simulated on the stretchable neuromorphic platform

Finally, we tested the AI-based-data analysis performance of a larger-scale intrinsically stretchable neuromorphic array, and studied the influence of mechanical stretching, through the simulated implementation of different types of algorithms based on the extracted performance of our device under different strain conditions (Tables S4-5). First, we compared the data analysis

performance of our device to other neuromorphic platforms on the standard AI benchmark MNIST (Modified National Institute of Standards and Technology) for hand-written digits recognition. The training accuracy (>95%) obtained with a simple 2-layer multilayer perceptron (MLP) model is very close to the ideal training performance with stochastic gradient descent (Figure S34). Next, to correlate our stretchable neuromorphic computing devices with wearable health monitoring applications, we applied AI data analysis based on ANNs constructed by extracting parameters from our device to the classification of ECG signals, using the Physionet's MIT-BIH Arrhythmia Dataset³⁷. The source of these ECGs was obtained by the Arrhythmia Laboratory at Beth Israel Hospital. Medically, ECGs can be classified into normal (N) and four abnormal classes (S, V, F, Q) based on the patterns in the timing and strength of the electrical signals (Figure 5A and Table S6), which can be utilized for the initial fast screening of cardiac disorders. From the full ECG Dataset, we created the largest possible balanced subset for validation, with 3200 training and 800 testing samples for each class. We first applied a 1-layer CNN model to the ECG dataset (Figure 5B and Experimental Procedures). With our model simulated on the neuromorphic platform under “stretching” from 0 to 100% strain (assuming a quasi-uniform distribution of strain on the simulated chip), the final training accuracy (achieved after 100 training epochs) remains at a high level around 90% (Figures 5C-D), which reveals the algorithmic robustness in the scaled device performance to changes from stretching. The training accuracy could even be further improved by using the full data set. Next, we studied the effect of device stretching on inference accuracy for the ECG classification. This is important because, for the practical scenarios we are envisioning, the stretch conditions will fluctuate during use, and they will in general be different from the condition under which the model was trained. The 5-by-5 confusion matrixes (Figures. 5E-H) illustrate the high classification accuracies on all the five classes of ECG signals. Notably, this

performance was consistently achieved whether the training and inference took place on the neuromorphic “chip” under the same or different strains. This, for the first time, clearly demonstrates the feasibility of running an ANN algorithm on a stretchable neuromorphic platform with the AI function minimally influenced by mechanical stretching on hardware, which is enabled by the linearity at both the device and algorithm levels: the neuromorphic transistor maintains high weight update linearity under different strains; and the AI model in use, CNN with the ReLU (Rectified Linear Unit) activation function, processes data in a piecewise linear fashion.

Besides CNN, we also built and tested a long short-term memory (LSTM) model (Figure S35A), which is more suitable for processing time-series signals such as ECG and other types of physiological signals. Under static strains from 0 to 100%, LSTM indeed achieved an even higher training accuracy of ~95% (Figure S35B-C). However, unlike CNN, when the strain-state difference between inference and training is greater than 20%, LSTM’s inference accuracy is observably compromised (Figure S36). This is due to the use of the non-linear tanh function as a part of the LSTM’s cell internal dynamics, and the recurrent nature of this architecture. This comparison suggests the emerging need for innovations in AI models for accommodating the linear weight scaling from the stretching of wearable neuromorphic chips while achieving high recognition accuracy for health-data-type time-series signals. This is a unique research opportunity in hardware-software co-design.

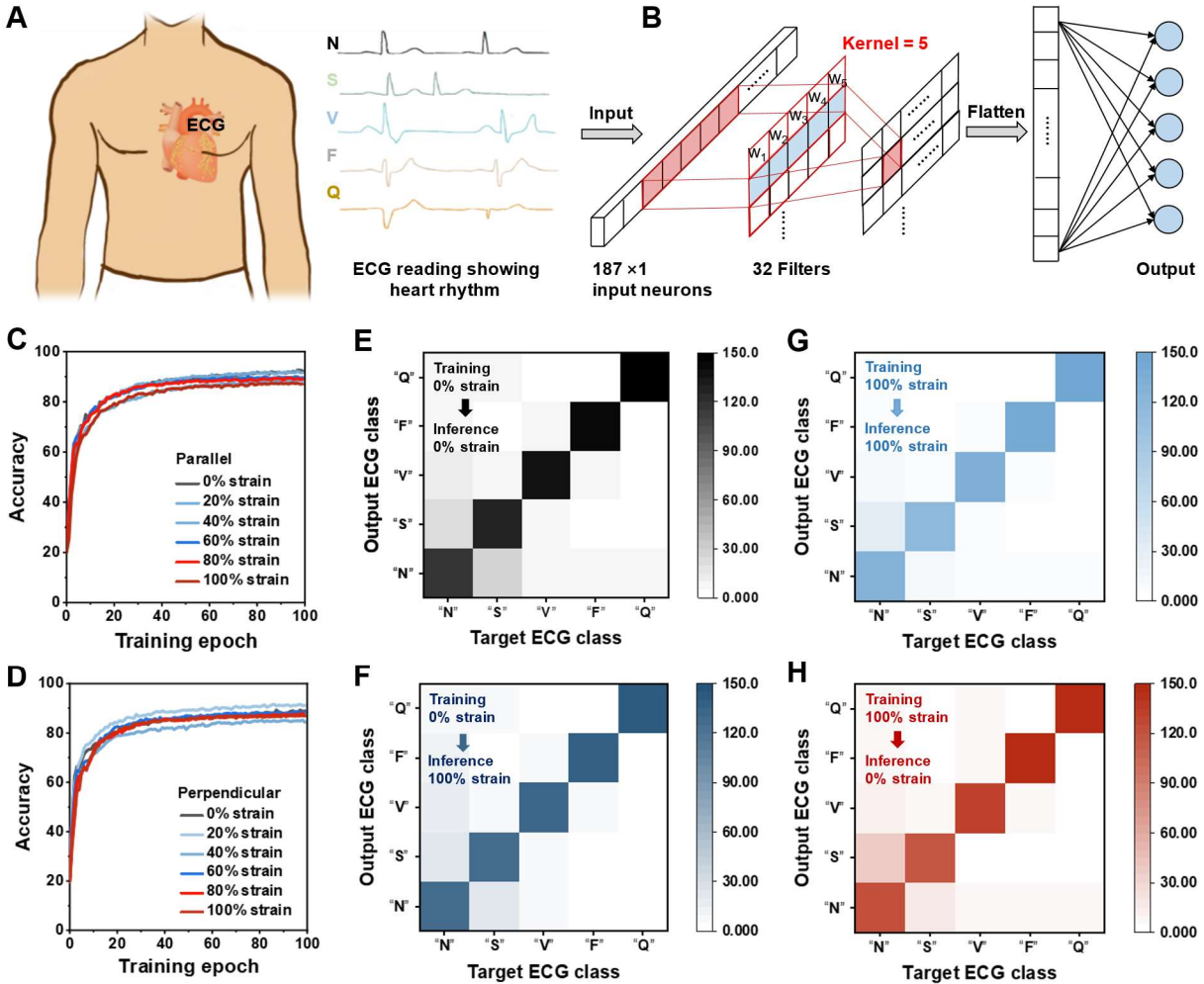


Figure 5. Simulated classification function for ECG patterns on the stretchable neuromorphic platform. (A) Schematics of five classes of human ECG waveforms: N, S, V, F, and Q. (B) A 1-layer convolution neural network with 187 input neurons, filter=32, kernel=5, and 5 output neurons. (C-D) Training curves at different strain conditions. (E-H) Confusion matrixes for a classification test of the ECG patterns at different strain levels.

Discussion

From the redox-active semiconducting polymer to the neuromorphic device and array, and finally AI-algorithmic functions, the high stretchability needed for on-skin integrations has been successfully combined with the neuromorphic-computing performance that is on par with the state

of the art. This streamline of research opens the path and lays the foundation for incorporating neuromorphic-computing-based AI analysis into wearable healthcare devices, in a skin-compatible and conformable form factor. Besides the neuromorphic devices, full neuromorphic systems typically also require peripheral circuits, for which stretchability could be realized based on the ongoing developments of stretchable FETs and circuits^{8,9} towards achieving more complicated circuit functions. Therefore, in the future research, further improvements of the integration level, the combination with other stretchable circuit components (e.g., switches, hardware-based neurons, and FET-based periphery circuits), and the co-design of new algorithms can lead to the realization of wearable devices for personalized, precision, and closed-loop healthcare, and also benefit other technology domains such as soft intelligent robots.

Experimental Procedures

Materials: p(gT2) ($M_w = 79.5$ kDa, PDI = 2.69, Figure S2) was synthesized according to a reported method in literature³⁸. Polymethyl methacrylate (PMMA, 495 A6, MicroChem Corp), (3-aminopropyl)trimethoxysilane (APTMS, 97%, Alfa Aesar), gold(III) chloride trihydrate (HAuCl_4 , Acros organics), sodium borohydride (NaBH_4 , 99%, Acros Organics), trisodium citrate dihydrate (99%, Alfa Aesar), 4-mercaptobenzoic acid (4-MBA, >95%, TCI), L-ascorbic acid (L-AA, Fisher Chemical) acrylamide monomer (TCI), N, N'-methylene(acrylamide) (99%, Sigma Aldrich), ammonium persulfate ($\geq 98\%$, Sigma Aldrich), N, N, N' N'-tetramethylethylenediamine (TEMED, $\sim 99\%$, Sigma Aldrich), benzophenone (Sigma Aldrich), silver/silver chloride (Ag/AgCl) silicone paste (Creative Materials), PDMS elastomer base and curing agent (Sylgard 184, Dow Corning), ethyl alcohol (200 proof, $\geq 99.5\%$, Sigma Aldrich), trimethylchlorosilane (TMS, Sigma Aldrich) were used as received.

Synthesis of Au-nanowire electrodes on a PDMS substrate: The Au-nanowires were synthesized

according to the reported methods³⁶ with some modifications (Figure S4). Firstly, the PMMA solution (495K A6) was spin-coated on a plasma-treated silicon wafer at a speed of 1500 rpm for 60 s, and then the sample was baked at 180 °C for 10 mins. After that, a PET tape-based shadow mask was laminated on the surface of PMMA, and then the sample was processed in plasma for several minutes. Subsequently, the shadow mask was removed, and the sample was immersed in an absolute ethanol solution of APTMS (6 $\mu\text{L}/\text{mL}$) for 2 h. After rinsing with ethanol and drying in a stream of nitrogen, the sample was immersed in the gold seed solution for another 2 h to anchor the gold seeds on the surface of the plasma-treated area of PMMA. The initial Au seed solution for Au-nanowire growth was prepared by reducing 0.25 mM HAuCl_4 with 6 mM NaBH_4 and 0.5 mM trisodium citrate dihydrate in an aqueous solution. After Au seed deposition, the sample was washed with DI water and dried with nitrogen flow. Then, the sample was immersed into Au-nanowire growth solution (ethanol/water: v/v=1), which contained a ligand MBA (1.1 mM), L-AA (16.4 mM), and HAuCl_4 (6.8 mM). After several minutes of growth, the samples were rinsed with ethanol and dried naturally under ambient conditions. PDMS base and curing agent were mixed (w/w = 15:1) and spin-coated on the sample at 400 rpm. After degassing, the sample was heated at 80°C for several hours. The PDMS was peeled off the sample, and the patterned vertical gold nanowire electrode was embedded in the PDMS film.

Preparation of organo-hydro-gel dielectric layers on the surface of PDMS: A prepared PDMS (base/curing agent: w/w = 15:1) thin film was washed thoroughly with methanol and DI water. Then, the surface of the PDMS thin film was pretreated by immersing the sample in a benzophenone solution (10 wt.% in ethanol) for 3 min at room temperature. After that, the PDMS thin film was washed three times with methanol and dried with nitrogen gas. The organo-hydro-gel was synthesized at the surface of the benzophenone treated PDMS. Briefly, 1.42 g acrylamide

monomer, 4.5 mg N, N'-methylene(acrylamide) cross-linker, 2.3 mg ammonium persulfate initiator, and 1.8 mg TEMED accelerator were dissolved in 10 mL DI water. The mixed solution was bubbled with nitrogen gas before being injected the solution into the mold at the surface of PDMS. After injection, the sample was put under UV light. After curing, the mold was removed, and the synthesized hydrogel was bonded firmly on the surface of PDMS. The sample is immersed in DI water for about 24 hours, and then immersed in a glycerol/water (3:1 v/v) mixed solution (containing 0.1 M NaCl) for 24 hours to obtain the final organo-hydro-gel.

Fabrication of stretchable neuromorphic devices: First, p(gT2) solution (6 mg/mL in chloroform) was spin-coated on octadecyltrimethoxysilane (OTS)-functionalized Si substrate at 500 rpm for 30 s, followed by annealing at 110°C for 1 h in the glovebox. Stretchable Ag/AgCl paste was blade coated onto the PDMS substrate with patterned vertical Au-nanowire electrodes. After the curing of the Ag/AgCl paste, the sample was plasma treated for 30 s. Then, the p(gT2) film was transferred onto the channel area of the patterned vertical Au-nanowire electrode. Finally, the organo-hydro-gel/PDMS thin film was laminated onto the top of the semiconductor and the gate. The packaging of the device was fabricated by pouring the PDMS solution (base/curing agent: w/w = 15:1) on the surface of the device and cured at room temperature.

Fabrication of neuromorphic device array: The manufacturing process of the array electrode is shown in Figure S5. The silicon wafer was treated with oxygen plasma and placed in a container with a small vial (1-2 mL) of TMS in a fume hood. The container was then sealed tightly, and the silicon wafer was exposed to TMS vapor for 2 h at room temperature. The sample was then taken out and washed with IPA and DI water followed by blow-drying with nitrogen gas. Subsequently, S1813 was spin-coated on the surface of the sample at 2000 rpm for 60 s followed by baking at 115 °C for 60 s. Electrode patterns were formed via a conventional photolithography process. After

exposure, the sample was immersed in developer solution for 60 s followed by immersing it in DI water for 60 s. Subsequently, the substrate was rinsed with DI water and dried by nitrogen flow. After that, the sample was treated with oxygen plasma for 4 mins. Then, S1813 was removed by immersing the sample in absolute ethanol solution for 5 mins. After that, the sample was directly immersed into the absolute ethanol solution of APTMS (6 $\mu\text{L}/\text{mL}$) for 2 h. After rinsing with ethanol and drying in a stream of nitrogen gas, the sample was immersed in the gold seed solution for another 2 h. After Au seed deposition, the sample was washed with DI water and dried with nitrogen flow. Then, the sample was immersed into an Au-nanowire growth solution. After several minutes of growth, the samples were rinsed with ethanol and dried naturally under ambient conditions. PDMS base and curing agent were mixed (w/w = 15:1) and spin-coated on the sample. After degassing, the sample was heated at 80°C until fully cured. The PDMS was peeled off the sample, and the patterned vertical gold nanowire electrode was embedded in the PDMS film. The patterned organo-hydro-gel was fabricated on a PDMS substrate with a mask (see Figure S31). Briefly, a prepared PDMS (base/curing agent: w/w = 15:1) thin film was washed thoroughly with methanol and DI water. Then, the PDMS thin film was pretreated by immersing the sample in a benzophenone solution (10 wt.% in ethanol) for 3 mins at room temperature. After that, the PDMS thin film was washed 3 times with methanol and dried with nitrogen gas. Then, a PET tape-based shadow mask was laminated on the surface of PDMS. Organo-hydro-gel precursor solution was added to the patterned area, and then another PET film was laminated on top. After UV curing, the mask was removed and the sample was soaked in DI water for 24 h, and then soaked in a glycerol-water binary solution (containing 0.1M NaCl) for another 24 h. The p(gT2) film was fabricated by spin-coating p(gT2) solution (6 mg/mL in chloroform) on top of the OTS-functionalized Si wafer at 500 rpm for 30 s, followed by annealing at 110°C for 60 min in the glovebox. After that, the

p(gT2) film was patterned through physical isolation by a razor. The device array was fabricated by firstly blade coating the Ag/AgCl paste onto the gate area of the array electrode. Then, the Ag/AgCl paste was cured at 80 °C for 40 mins. Subsequently, the sample was treated with oxygen plasma for 30 s. After that, PDMS was used to transfer the patterned p(gT2) film to the channel area of the array electrode. Finally, the patterned organo-hydro-gel was laminated on the sample to complete the array manufacturing.

Device characterization: The basic OECT performance was done by using a Keithley 4200 semiconductor system. The neuromorphic performance was measured by using a Keithley 4200 semiconductor system, two dual-channel Rigol DG 4162 function generators, a Keithley 6514 Programmable Electrometer, a National Instruments NI-DAQ, and custom-built circuits using commercial off-the-shelf components. Specifically, the stretchability and the long-term storage stability tests of the neuromorphic transistors were done by using the Keithley 4200 semiconductor system. During testing, a 10 M Ω resistor was connected in series with the gate of the neuromorphic device to ensure that no unintentional loss of state occurs. The devices were tested by applying 400 consecutive potentiation pulses in -2.5 V and 200 ms, followed by 400 consecutive depression pulses in 1.3 V and 200 ms, to the gate through the resistor. Before testing, all devices were programmed to have the similar initial conductivity. Other neuromorphic performances, including dynamic range, switching endurance, reproducibility of conductance change, array performance, were collected by using two dual-channel Rigol DG4162 function generators, a Keithley 6514 Programmable Electrometer, a National Instruments NI-DAQ, and custom-built circuits using commercial off-the-shelf CMOS switches (MAX4522ESE+).

Machine learning model architecture: The training and inference of the deep neural networks in this work were implemented using deep learning frameworks TensorFlow³⁹ and PyTorch⁴⁰. The

MLP model for the MNIST classification task includes two hidden layers of size 64 and 32, and an output layer with size 10, consisting of $50240 + 2080 + 330 = 52650$ weight and bias parameters. The LSTM model for the ECG signal classification task includes a standard LSTM module and an attention head over the time dimension, consisting of $40800 + 9505 = 50305$ parameters. The CNN model for the ECG signal classification task includes a convolution layer with 32 filters and kernel size 5, followed by a flatten layer, a hidden layer of size 32, and an output layer of size 5. It consists of $192 + 187424 + 165 = 187781$ parameters. All the model parameters are trainable. For reference performance, these models were trained using standard backpropagation with the stochastic gradient descent (SGD) algorithm⁴¹ implemented in the deep learning frameworks.

Weight update with Manhattan Rule: Neuromorphic devices use conductance to encode model parameters¹⁶. Because conductance cannot be negative, two conductance values are needed to express the full range of a synaptic weight. In our simulation, following the convention in analog training, we encode the weight as the difference between the conductance of two devices ($W = G^+ - G^-$). The synaptic weight can thus be updated by adjusting the corresponding pair of conductance states through potentiation or depression. For example, if the weight needs to be strengthened, G^+ increases and G^- decreases at the same time with the application of LTP/LTD pulses, thereby increasing the synaptic weight. However, unlike the SGD algorithm, Manhattan Rule⁴² for analog training only uses the sign information for the needed weight update; the magnitude of weight change is fixed following an update pulse. For our neuromorphic device, the change amount depends on both the device's strain state (i.e., strain) and the current conductance value. Specifically, the increase and decrease of G^+/G^- is determined by the following equations⁴³:

$$G_{n+1} = G_n + \Delta G_P = G_n + \alpha_P e^{-\beta_P \frac{G_n - G_{min}}{G_{max} - G_{min}}}, (G^+ \text{ or } G^- \uparrow)$$

$$G_{n+1} = G_n + \Delta G_D = G_n - \alpha_D e^{-\beta_D \frac{G_{max} - G_n}{G_{max} - G_{min}}}, (G^+ \text{ or } G^- \downarrow)$$

where G_n and G_{n+1} stand for the synaptic conductance before and after the n^{th} pulse is applied, and the material parameters α and β help model the conductance change amount and the nonlinearity, respectively (Tables S3-4). All the parameters in these equations (α , β , G_{\min} , G_{\max}) were extracted by fitting the LTP/D curve of our devices.

Weight update with Cumulative Manhattan Rule: Manhattan Rule is a weaker version of the backpropagation algorithm: by using only the sign of the gradient⁴², it is ineffective at dealing with situations where the needed update amounts differ substantially among all the parameters in a network. To combat this problem, we designed a variation of the Manhattan Rule, called Cumulative Manhattan Rule, to simulate the training of the neural network. The key intuition is to improve the resolution of weight updates by accumulating gradients across batches. Our variant uses the sign of the sum of all gradients during the current training period. Whereas the original Manhattan algorithm discards magnitude between batches, ours preserves this information. For example, if a large positive gradient is followed by many small negative ones, the original method would apply more negative changes, resulting in an overall update in the wrong direction. Our algorithm, in contrast, would keep the right direction by tracking the aggregate gradients. Simulation results show that our algorithm generally converges faster and achieves better performance on all the models we experimented with. Therefore, all simulation results in this work were obtained based on our Cumulative Manhattan Rule.

Simulation of the strain impact on machine learning: Under different strain conditions, the device conductance responds to pulses differently. This relationship is modeled by the equations in the previous section on weight updates. By subjecting the material to a wide range of strain conditions and recording the pulse response curves, we extracted the parameters (α , β , G_{\min} , G_{\max}) for each strain condition, and stored in a lookup table. Thus, to simulate the impact of a constant

strain, we only need to look up the parameters from the table and apply the conductance updates accordingly in the simulation of model training. If the strain changes, all weights will be affected. The new conductance value is obtained by scaling the original value by a constant factor, which is roughly estimated from the transfer curve measured under different strains (Figure S21). The scaling factor between two strain conditions is derived by averaging the ratio of experimentally recorded conductance values in the same range.

Acknowledgements: This work is supported by the US Office of Naval Research (N00014-21-1-2266, N00014-21-1-2581), the National Science Foundation award DMR-2011854, and the start-up fund from the University of Chicago. This research used resources of the Advanced Photon Source, a US Department of Energy Office of Science User Facility, operated for the Department of Energy Office of Science by Argonne National Laboratory under contract DE-AC02-06CH11357. J.X. acknowledges the Center for Nanoscale Materials, a US Department of Energy Office of Science User Facility and supported by the US Department of Energy Office of Science, under contract DE-AC02-06CH11357. We appreciate the kind discussion with Q. Xia at University of Massachusetts at Amherst.

Author contributions: S. Wang conceived and supervised this study. S.D. and S. Wang designed the experiments. S. D. and Y. D. performed the material synthesis, characterizations, device fabrications and measurements. Z. Z., F. X., and R. S. performed the simulation. S. D., Y. Li, Y. Liu. and S. L. fabricated the stretchable vertical Au-nanowire-based electrodes. Y. D. and J. S. helped with the GXID measurement. S. D., Y. Li. and P. C. set up the testing system. Y. Li helped with the organo-hydro-gel fabrication and P.C. helped with tensile testing of the organo-hydro-gel. N. L., Q. S., S. Wai, W. L., C. Z., J. Y., J. J. Y. and J. X. helped with the data analyses. S. D., S. Wang, F.X., and Y.D. wrote the manuscript. All authors reviewed and commented on the

manuscript.

Competing interests: The authors declare no competing interests.

Data availability: The data that support the findings of this study are available from the corresponding author on reasonable request.

References:

1. Mesko, B. (2017). The role of artificial intelligence in precision medicine. *Expert Rev. of Precis. Med. Drug Dev.* 2, 239-241. 10.1080/23808993.2017.1380516.
2. Gao, W., Emaminejad, S., Nyein, H., Challa, S., Chen, K., Peck, A., Fahad, H. M., Ota, H., Shiraki, H., Kiriya, D., et al. (2016). Fully integrated wearable sensor arrays for multiplexed in situ perspiration analysis. *Nature* 529, 509-514. 10.1038/nature16521.
3. Yu, K.-H., Beam, A. L., Kohane, I. S. (2018). Artificial intelligence in healthcare. *Nat. Biomed. Eng.* 2, 719-731. 10.1038/s41551-018-0305-z.
4. Jung, D., Lim, C., Shim, H., Kim, Y., Park, C., Jung, J., Han, S., Sunwoo, S.-H., Cho, K., Cha, G., et al. (2021). Highly conductive and elastic nanomembrane for skin electronics. *Science* 373, 1022-1026. 10.1126/science.abh4357.
5. Matsuhisa, N., Inoue, D., Zalar, P., Jin, H., Matsuba, Y., Itoh, A., Yokota, T., Hashizume, D., Someya, T. (2017). Printable elastic conductors by in situ formation of silver nanoparticles from silver flakes. *Nat. Mater.* 16, 834-840. 10.1038/nmat4904.
6. You, I., Mackanic, D. G., Matsuhisa, N., Kang, J., Kwon, J., Beker, L., Mun, J., Suh, W., Kim, T., Jeffrey Tok, J. B.-H., et al. (2020). Artificial multimodal receptors based on ion relaxation dynamics. *Science* 370, 961-965. 10.1126/science.aba5132.
7. Yu, X., Xie, Z., Yu, Y., Lee, J., Vazquez-Guardado, A., Luan, H., Ruban, J., Ning, X., Akhtar, A., Li, D., et al. (2019). Skin-integrated wireless haptic interfaces for virtual and

- augmented reality. *Nature* 575, 473-479. 10.1038/s41586-019-1687-0.
8. Wang, S., Xu, J., Wang, W., Wang, G.-J., Rastak, R., Molina-Lopez, F., Chung, J., Niu, S., Feig, V. R., Lopez, J., et al. (2018). Skin electronics from scalable fabrication of an intrinsically stretchable transistor array. *Nature* 555, 83-88. 10.1038/nature25494.
 9. Wang, W., Wang, S., Rastak, R., Ochiai, Y., Niu, S., Jiang, Y., Arunachala, P., Zheng, Y., Xu, J., Matsuhisa, N., et al. (2021). Strain-insensitive intrinsically stretchable transistors and circuits. *Nat. Electron.* 4, 143-150. 10.1038/s41928-020-00525-1.
 10. Zhou, F. & Chai, Y. (2020). Near-sensor and in-sensor computing. *Nat. Electron.* 3, 664-671. 10.1038/s41928-020-00501-9.
 11. Covi, E., Elisa Donati, E., Liang, X., Kappel, D., Heidari, H., Payvand, M., Wang, W. (2021). Adaptive Extreme Edge Computing for Wearable Devices. *Front. Neurosci.* 15, 611300. 10.3389/fnins.2021.611300.
 12. Zheng, Y. Q., Liu, Y., Zhong, D., Nikzad, S., Liu, S., Yu, Z., Liu, D., Wu, H.-C., Zhu, C., Li, J., et al. (2021). Monolithic optical microlithography of high-density elastic circuits. *Science* 373, 88-94. 10.1126/science.abh3551.
 13. Tuma, T., Pantazi, A., Gallo, M. Le, Sebastian, A. & Eleftheriou, E. (2016). Stochastic phase-change neurons. *Nat. Nanotech.* 11, 693-699. 10.1038/nnano.2016.70.
 14. Mou, X., Tang, J., Lyu, Y., Zhang, Q., Yang, S., Xu, F., Liu, W., Xu, M., Zhou, Y., Sun, W., et al. (2021). Analog memristive synapse based on topotactic phase transition for high-performance neuromorphic computing and neural network pruning. *Sci. Adv.* 7, eabh0648. 10.1126/sciadv.abh0648.
 15. Ohno, T., Hasegawa, T., Tsuruoka, T., Terabe, K., Gimzewski, J. K., Aono, M. (2011). Short-term plasticity and long-term potentiation mimicked in single inorganic synapses.

- Nat. Mater. *10*, 591-595. 10.1038/nmat3054.
16. Prezioso, M., Merrih-Bayat, F., Hoskins, B. D., Adam, G. C., Likharev, K. K., Strukov, D. B. (2015). Training and operation of an integrated neuromorphic network based on metal-oxide memristors. *Nature* *521*, 61-64. 10.1038/nature14441.
 17. Zidan, M. A., Strachan, J. P. & Lu, W. D. (2018). The future of electronics based on memristive systems. *Nat. Electron.* *1*, 22-29. 10.1038/s41928-017-0006-8.
 18. Gkoupidenis, P., Koutsouras, D. A., Malliaras, G. G. (2017). Neuromorphic device architectures with global connectivity through electrolyte gating. *Nat. Commun.* *8*, 15448. 10.1038/ncomms15448.
 19. Kim, Y., Chortos, A., Xu, W., Liu, Y., Oh, J., Son, D., Kang, J., Foudeh, A. M., Zhu, C., Lee, Y., et al. (2018). A bioinspired flexible organic artificial afferent nerve. *Science* *360*, 998-1003. 10.1126/science.aao0098.
 20. van de Burgt, Y., Melianas, A., Keene, S. T., Malliaras, G., Salleo, A. (2018). Organic electronics for neuromorphic computing. *Nat. Electron.* *1*, 386-397. 10.1038/s41928-018-0103-3.
 21. Lee, Y., Oh, J., Xu, W., Kim, O., Kim, T., Kang, J., Kim, Y., Son, D., Tok, J. B.-H., Park, M., et al. (2018). Stretchable organic optoelectronic sensorimotor synapse. *Sci. Adv.* *4*, eaat7387. 10.1126/sciadv.aat7387.
 22. Shim, H., Sim, K., Ershad, F., Yang, P., Thukral, A., Rao, Z., Kim, H.-J., Liu, Y., Xu Wang, X., Gu, G., et al.(2019). Stretchable elastic synaptic transistors for neurologically integrated soft engineering systems. *Sci. Adv.* *5*, eaax4961. 10.1126/sciadv.aax4961.
 23. Kim, S., Baek, G., Yoon, J., Seo, S., Park, J., Hahm, D., Chang, J., Seong, D., Seo, H., Oh, S., et al. (2021). A bioinspired stretchable sensory-neuromorphic system. *Adv. Mater.* *33*,

2104690. 10.1002/adma.202104690.
24. van de Burgt, Y., Lubberman, E., Fuller, E. J., Keene, S. T., Faria1, G. C., Agarwal, S., Marinella, M. J., Talin, A. A., Salleo A. (2017). A non-volatile organic electrochemical device as a low-voltage artificial synapse for neuromorphic computing. *Nat. Mater.* *16*, 414-418. 10.1038/nmat4856.
 25. Fuller, E. J., Keene, S. T., Melianas, A., Wang, Z., Agarwal, S., Li, Y., Tuchman, Y., James, C. D., Marinella, M. J., Yang, J. J., et al. (2019). Parallel programming of an ionic floating-gate memory array for scalable neuromorphic computing. *Science* *364*, 570-574. 10.1126/science.aaw5581.
 26. Fuller, E. J., Li, Y., Bennet, C., Keene, S. T., Melianas, A., Agarwal, S., Marinella, M. J., Salleo, A., Talin A. A. (2019). Redox transistors for neuromorphic computing. *Ibm J. Res. Dev.* *63*, 9:1-9:9. 10.1147/JRD.2019.2942285.
 27. Lee, W., Kobayashi, S., Nagase, M., Jimbo, Y., Saito, I., Inoue, Y., Yambe, T., Sekino, M., Malliaras, G. G., Yokota, T., et al. (2018). Nonthrombogenic, stretchable, active multielectrode array for electroanatomical mapping. *Sci. Adv.* *4*, eaau242. 10.1126/sciadv.aau2426.
 28. Matsuhisa, N., Jiang, Y., Liu, Z., Chen, G., Wan, C., Kim, Y., Kang, J., Tran, H., Wu, H.-C., You, I., et al. (2019). High-transconductance stretchable transistors achieved by controlled gold microcrack morphology. *Adv. Electron. Mater.* *5*, 1900347. 10.1002/aelm.201900347.
 29. Zhang, S., Li, Y., Tomasello, G., Anthonisen, M., Li, X., Mazzeo, M., Genco, A., Grutter, P., Fabio Cicoira, F. (2019). Tuning the electromechanical properties of PEDOT:PSS films for stretchable transistors and pressure sensors. *Adv. Electron. Mater.* *5*, 1900191.

- 10.1002/aelm.201900191.
30. Li, Y., Zhang, S. M., Li, X. D., Unnava, V. R. N. & F. Cicoira, (2019). Highly stretchable polystyrene sulfonate organic electrochemical transistors achieved via polyethylene glycol addition. *Flex. Print. Electron.* *4*, 044004. 10.1088/2058-8585/ab5202.
 31. Tan, S., Gumyusenge, A., Melianas, A., Moser, M., Cotts, B., Singh, D., McCulloch, I., Salleo, A. (2021). High-gain chemically gated organic electrochemical transistor. *Adv. Funct. Mater.* *31*, 2010868. 10.1002/adfm.202010868.
 32. Dai Y., Dai, S., Li, N., Li Y., Moser, M., Strzalka, J., Prominski, A., Liu, Y., Zhang, Q., Li, S., et al. (2022). Stretchable redox-active semiconducting polymers for high-performance organic electrochemical transistors. *Adv. Mater.* 2201178. 10.1002/adma.202201178.
 33. Paulsen, B., Tybrandt, K., Stavrinidou, E., Rivnay, J. (2020). Organic mixed ionic–electronic conductors. *Nat. Mater.* *19*, 13–26. 10.1038/s41563-019-0435-z.
 34. Han, L., Liu, K., Wang, M., Wang, K., Fang, L., Chen, H., Zhou, J., Lu, X. (2018). Mussel-inspired adhesive and conductive hydrogel with long-lasting moisture and extreme temperature tolerance. *Adv. Funct. Mater.* *28*, 1704195. 10.1002/adfm.201704195.
 35. Lane, L. B.(1925). Freezing points of glycerol and its aqueous solutions, *Ind. Eng. Chem.*, *17*, 924-924. 10.1021/ie50189a017.
 36. Zhu, B., Gong, S., Lin, F., Wang, Y., Ling, Y., An, T., Cheng W. (2019). Patterning Vertically grown gold nanowire electrodes for intrinsically stretchable organic transistors. *Adv. Electron. Mater.* *5*, 1800509. 10.1002/aelm.201800509.
 37. Moody, G. & Mark, R. (2001). The impact of the MIT-BIH arrhythmia database. *IEEE Eng. Med. Biol. Mag* *20*, 45-50. 10.1109/51.932724.
 38. Moia, D., Giovannitti, A., Szumska, A. A., Maria, I. P., Rezasoltani, E., Sachs, M., Schnurr,

- M., Barnes, P. R. F., McCulloch, I., Nelson, J. (2019). Design and evaluation of conjugated polymers with polar side chains as electrode materials for electrochemical energy storage in aqueous electrolytes. *Energy Environ. Sci.* *12*, 1349-1357. 10.1039/C8EE03518K.
39. Abadi, M., Barham, P., Chen, J., Chen, Z., Davis, A., Dean, J., Devin, M., Ghemawat, S., Irving, G., Isard, M. et al. (2016). Tensorflow: A system for large-scale machine learning. [arXiv:1605.08695](https://arxiv.org/abs/1605.08695).
40. Adam P., Gross, S., Massa, F., Lerer, A., Bradbury, J., Chanan, G., Killeen, T., Lin, Z., Gimelshein, N., Antiga, L., et al. (2019). PyTorch: an imperative style, high-performance deep learning library. [arXiv:1912.01703](https://arxiv.org/abs/1912.01703).
41. Ruder, S. (2017). An overview of gradient descent optimization algorithms. [arXiv:1609.04747](https://arxiv.org/abs/1609.04747).
42. Zamanidoost, E., Bayat F. M., Strukov D. & Kataeva, I. Manhattan rule training for memristive crossbar circuit pattern classifiers. (2015). 2015 IEEE 9th International Symposium on Intelligent Signal Processing (WISP) Proceedings, 1-6. 10.1109/WISP.2015.7139171.
43. Choi, Y., Oh, S., Qian, C., Park, J.-H. & Cho, J. H. (2020). Vertical organic synapse expandable to 3D crossbar array. *Nat. Commun.* *11*, 4595. 10.1038/s41467-020-17850-w.